

Supporting Information:

The Role of Optical Projection in the Analysis of Membrane Fluctuations

S. Alex Rautu¹, Davide Orsi², Lorenzo Di Michele³, George Rowlands¹, Pietro Cicuta^{3,*}, Matthew S. Turner^{1,†}

¹ *Department of Physics, University of Warwick, Coventry, CV4 7AL, United Kingdom*

² *Department of Mathematics, Physics and Computer Sciences, University of Parma, Italy*

³ *Cavendish Laboratory, University of Cambridge, Cambridge, CB3 0HE, United Kingdom*

* pc245@cam.ac.uk † m.s.turner@warwick.ac.uk

S.1 Methods

Sample preparation

The GUVs have been prepared by means of electroformation, following the procedure detailed in the supplementary information of reference [1]. We use DOPC and the fluorescently labelled lipid Texas Red DHPE (1,2-dihexadecanoyl-sn-glycero-3-phosphoethanolamine, triethylammonium salt), both from Avanti Polar Lipids, which were dissolved in chloroform in proportions 99.2% – 0.8%wt, and the final concentration of the solution was 25 mg mL⁻¹. A drop (20 μL) of solution was spin coated on half of the surface of an Indium Tin Oxide (ITO) coated glass slide at 60°C, prewet with isopropanol. The slide is then put in a desiccator, under low vacuum for 1 h. The lipid-covered portion of ITO slide, a second ITO slide and a plastic U-shaped spacer (AlteSil™ Silicone) were arranged to form a capacitive cell, with the ITO-covered surfaces facing the interior. The cell was filled with a 197 mM sucrose solution and then sealed with parafilm. A sinusoidal electric potential with frequency of 10 Hz, and peak-to-peak tension of 1 V was applied across the cell for 2 hours, after which the frequency was reduced to 2 Hz for 1 hour. The electric field promotes hydration, generating GUVs, and subsequent detachment from the lipid-covered ITO slide [2]. The resulting GUV suspension was diluted in a 200 mM glucose solution in 1:9 proportion and stored at 4°C in a plastic vial. Vesicles were used within 2 days.

Scanning confocal microscopy

The microscopy experiments were performed using a Leica TCS SP5 II confocal scanning inverted microscope on vesicles that are sedimented to the bottom of the measurement chamber; the reason for this is practical, as the sedimentation of GUVs minimises their diffusive motion in the suspension. The microscope is equipped with an HCX PL APO CS 40.0× oil immersion objective with numerical aperture NA = 1.30. Illumination is provided by a $\lambda = 594$ nm He-Ne laser. Experiments are carried out at room temperature $T = 22^\circ\text{C}$. We calibrated for the dependence of the focal depth (namely, the width of the fitted Gaussian to the intensity profile along the z -direction, out of the focal plane) with the pinhole size, as shown in Fig. S.1a. Also, we measured the Gaussian width of the point spread function in the focal plane as function of the pinhole size, see Fig. S.1b.

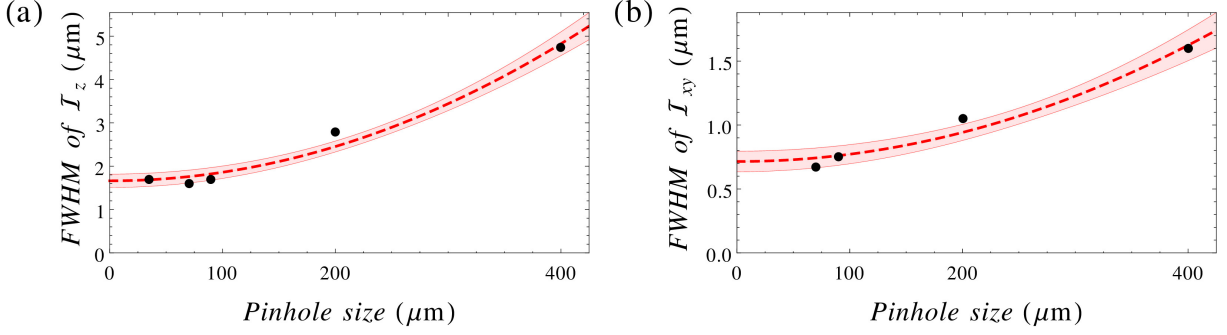


Figure S.1. Experimentally measured full widths at half maximum (FWHMs) of the intensity profiles: (a) along the z -direction (out of the focal zone), and (b) within the xy plane (i.e. the focal plane), both as a function of the pinhole size of the microscope. The red dashed line is a quadratic fitting, with a vanishing gradient at zero pinhole size.

The illumination spot is raster-scanned across the field of view at a line frequency $\nu = 8$ kHz. The acquisition time of a point of the projected membrane $\tau \simeq \mathcal{W} / \nu$ ranges between 1–2 ms in our experiments, where $\nu = p \nu$ is the effective velocity of the line scanning front, perpendicular to the scan direction, and \mathcal{W} is the lateral width of the illumination spot. This non-synchronous acquisition leads to a cutoff in the mode spectrum, $q \lesssim \mathcal{Q}$, given by the condition that the mode half-lifetime associated to the highest (fastest relaxation) mode, from Eq. (S.2.20), should be longer than the time to scan across its wavelength; namely, define \mathcal{Q} by $\frac{1}{2} \tau_{\mathcal{Q}} \equiv 2\pi R / (\nu \mathcal{Q})$. Thus, we can assume that each portion of the raster scan of size $2\pi R / \mathcal{Q}$ samples membrane configurations from an equilibrium distribution, whereas the amplitudes on separate slices may have become temporally decorrelated. We typically obtain $\mathcal{Q} \approx 20$.

We performed a numerical study to evaluate specifically scanning artefacts, with respect to the use of a common confocal microscope. Using a standard Metropolis Monte Carlo (MC) [3], we simulate in 2D a periodic fluctuating string of $N = 100$ particles interacting with harmonic stretching and bending potentials. The x -coordinate of each particle is constrained to a distance l (equal to the equilibrium bond length) from its neighbours, while the y -coordinate is allowed to fluctuate, so that the total energy of the system is

$$E = \sum_{i=1}^N \frac{1}{2} \alpha \left[\sqrt{(y_{i+1} - y_i)^2 + l^2} - l \right]^2 + \sum_{i=1}^N \frac{1}{2} \beta \theta_i^2, \quad (\text{S.1.1})$$

where $\alpha l^2 = \beta = 10 k_B T$, y_i is the y -coordinate of the i th particle, θ_i is the angle formed by the bonds of the i th particle with its neighbours (with $N + 1 \equiv 1$ to enforce periodicity). Fig. S.2(a) shows the mean-squared amplitude of the string's fluctuation spectrum averaged over a trajectory of 2×10^6 MC cycles, each corresponding to 100 individual displacement moves along the y direction (with a maximum amplitude equal to l). As expected for a fluctuating line with this physics, the spectrum follows q^{-2} and q^{-4} regimes, which mirrors the curves found for projected membrane fluctuations (slopes between q^{-1} and q^{-3}). In general, MC is unsuitable to generate realistic dynamics. However, in multiple instances it has been demonstrated theoretically numerically how MC trajectories reproduce accurately Brownian dynamics if hydrodynamic interactions are negligible and MC moves are local and have small amplitude [4, 5]. In our case, this is reflected by Fig. S.2(b), where we plot the q dependence of the mode decay

time τ , expressed in units of 10 MC cycles. As expected $\tau(q)$ monotonically decreases.

The fluctuating-string trajectory is used to generate the (binary) video of a fluctuating circle mimicking the contour of a GUV. This “full framerate” video, is then re-sampled simulating the raster-scanning of a confocal microscope operating at different speeds, to create a series of videos that faithfully reproduce potential artefacts. These circles are then converted back to strings, and their fluctuation spectra compared to the originally simulated one.

In Fig. S.2(c) we show such comparison, expressing the simulated imaging framerate R_{sc} in units of the inverse decay time of fluctuation mode $q = 2$ ($\tau(2)$). As the framerate drops, the spectra deviate from the reference curve, with the amplitude of high- q modes being artificially increased by contour disruption caused by scanning. As expected, lower framerates cause lower- q modes to be affected. Using the scanning framerate of our experimental setup, and estimating $\tau(2)$ from Eq. 2 of the main text using the values of k and $\bar{\sigma}$ obtained by the fitting reported in figure 2a, we find $R_{sc} \tau(2) \approx 14.7$. At this framerate, Fig. S.2(c) predicts negligible deviations of the “scanned” spectrum from the ideal one for $q \lesssim 20$. This value is not dissimilar from the one estimated theoretically, despite the similarities between the MC-simulated trajectory and the experimental data are only qualitative (the former are generated from the fluctuations of a string rather than a membrane). One should also note that in our data analysis algorithm the upper boundary q_{max} of the fitted q -interval is chosen as the one that maximises the posterior probability (see SI section S.3). Typically this optimal value is around 13-14 (see Fig. S.6), thus smaller than \mathcal{Q} . Naively, one may find surprising how, in scanning mode, an accurate sampling of the contour can still be achieved even when imaging at relatively low framerates. For instance, bright field videos for flickering are recorded at much greater speed, typically exceeding 230 fps, as compared to the 15 fps of our confocal. This apparent paradox is however resolved if one considers that in scanning mode the image is reconstructed line by line. As explained when deriving our theoretical estimate of \mathcal{Q} , what matters for the accurate sampling of each fluctuation mode is that the imaging front covers a distance equal to the fluctuation wavelength faster than the decay rate of the mode. Since fast-decaying modes also have smaller wavelengths, they can be effectively sampled even if the time require to capture an entire frame is much larger than their decay time τ . To exemplify this, in Fig. S.2(c) we compare the effects of scanning with a “global shutter” imaging used in bright field videos, where fluctuations are averaged over a time equal to the inverse framerate (or the shutter time, if smaller). It is immediately clear how for a given framerate, the artefacts of a global shutter are significantly more severe and lead to an apparent suppression of the fluctuations.

Fluctuation spectrum

In order to retrieve the fluctuation spectrum from the videos of the vesicles, the position of the contour points in every frame have to be determined with sub-pixel resolution. Typically, in case of phase-contrast videos, the membrane position is determined by finding the inflection point in the radial intensity profile, as in [6]. In case of fluorescence videos, the maximum of the intensity profile is commonly used to mark the membrane position. Building on our previous methods [7], we developed a refined algorithm based on template correlation to detect the contour position independently from the imaging mode employed

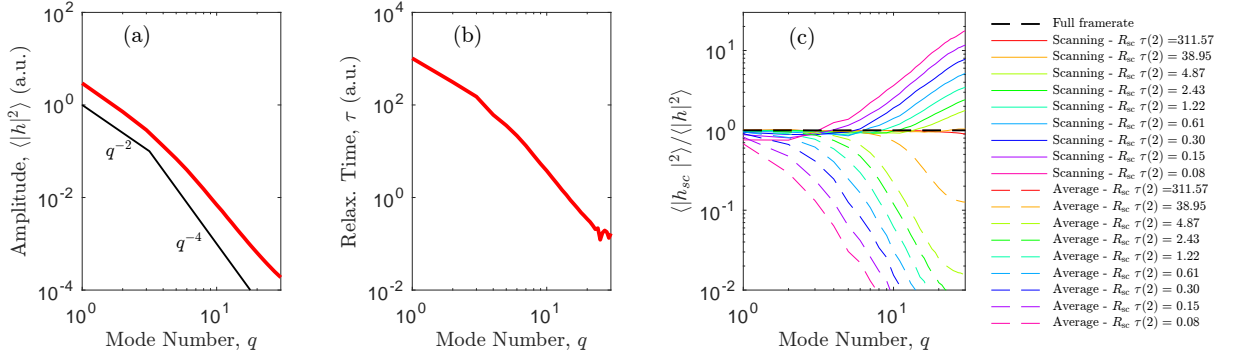


Figure S.2. Simulating scanning and averaging artefacts on the imaging of fluctuating vesicles. (a) Fluctuation spectrum of a bead-and-spring chain simulated by Metropolis MC. (b) Correlation time of the fluctuation modes in units of 10 MC cycles. (c) Ratio between the fluctuation spectra from finite-framerate imaging simulations and the “full-framerate” spectrum of panel (a). Solid lines mark imaging performed by raster scanning, imitating a scanning laser confocal microscope. Dashed lines indicate global-shutter imaging (simple time averaging). Framerate R_{sc} is expressed in units of the decay mode $\tau(2)$.

to acquire the videos. The results of the two methods are identical. The contour is typically expressed in polar coordinates (r, φ) with respect to the centre of the vesicle. The algorithm is as follows:

1. the centre and radius R of the vesicle are manually selected on the first frame (Fig. S.3a);
2. a ring region $C(r, \varphi)$ centred around the contour (namely, a strip in polar coordinates) of appropriate width is extrapolated from the image, by using a cubic interpolation;
3. a template of the radial profile is calculated from the ring of the first frame through an automatic averaging procedure (Fig. S.3b); then, we compute the two-dimensional correlation $U(r, \varphi)$ of the template with the contour ring itself. Here, $U(r, \varphi)$ is given by the point where the profile measured at each φ has maximum correspondence with the template.
4. the measurement of the radial position of the contour, say $\rho(\varphi)$, is obtained by a parabolic fitting of U around its maximum for every value of φ (Fig. S.3c).

The algorithm cycles three times from point 2 up to point 4, each time refining the estimate of the centre of vesicle and mean radius R , using the previously obtained contour (Fig. S.3d). The procedure is repeated for every frame, using the centre and mean radius calculated for the previous frame as the starting point for the current frame. The contour $\rho(\varphi, t)$ is then saved as a 2D array, as shown in (Fig. S.3e). The spectrum of contour fluctuations about the mean radius is calculated using a *Fast Fourier Transform* algorithm (e.g. in Matlab).

Spectrum fitting

The data analysis described in the main text is implemented as a Mathematica routine (DataAnalysis.nb). The file is divided into sections.

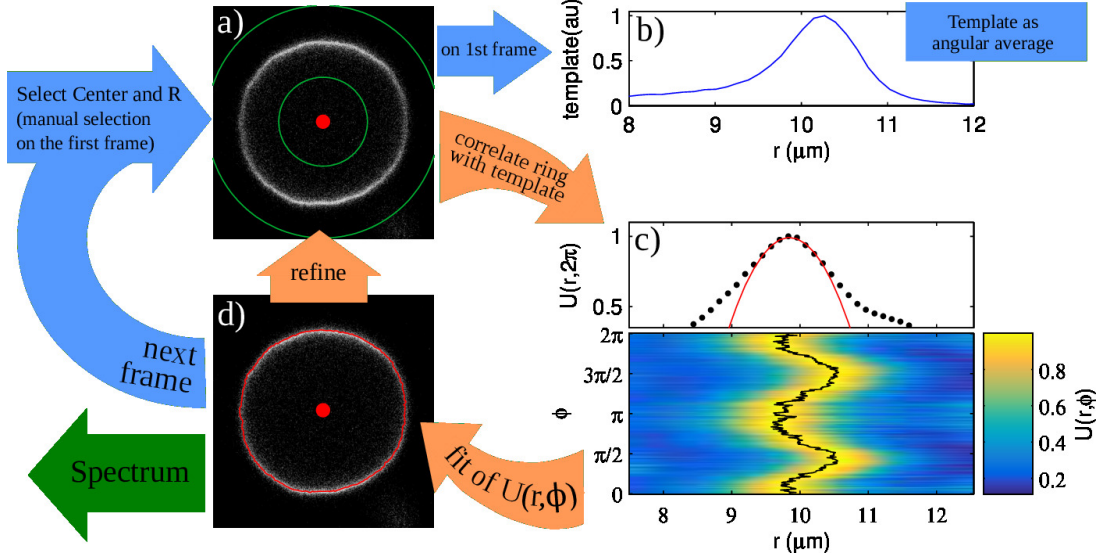


Figure S.3. In clockwise order: a) from the last estimate of center and mean radius R , a ring region around the equator of the vesicle is selected using cubic interpolation. In the first frame, center and R are manually selected. b) the ring measured on the first frame is averaged along φ to calculate a template. This used to calculate the two-dimensional correlation $U(r, \varphi)$ of the template with the contour ring itself. c) At each value of φ , the contour position is calculated via parabolic fitting of $U(r, \varphi)$. d) The position of the contour of the vesicle is used to refine the position of the center and the value of R . The algorithm cycles (orange arrows) three times between points b)–d), then it skips to the next frame.

- In the “Definitions” section, the theoretical expression of the mean square amplitude $\langle \bar{\mu}_q(t) \bar{\mu}_q^*(t) \rangle$ is set as in Eq. (S.2.38).
- The values of the focal depth and of the point-spread function of the microscope as a function of the confocal pinhole size must be provided in the “Calibration Data” section.
- The experimental data are loaded (“Experimental Data” section). The fluctuation spectrum of the GUV calculated using the Matlab algorithm is exported as a text file in json format. Several examples are provided along with the analysis code in the folder “DataExample”.
- The best-fit parameters to the experimental data are found by means of a maximum likelihood estimate defined as the minimisation of $\chi_\Delta^2(\kappa, \bar{\sigma})$, defined in Eq. (S.3.1). An example of its use is reported in the file.
- The file also contains a function that performs the fit while finding the best q -range for the fit, according to the maximization of the posterior probability defined in Eq. (S.3.9). This function yield more accurate results when several measurements at different values of Δ are available. These measurements can either be the same vesicle measured using several values of focal depth, different vesicles (with different R) measured at fixed focal depth, or both.

For the routine to work effectively, the necessary calibration data (see the “Confocal microscopy” section) are necessary. Some minor modifications might be required to specify the exposure time and the

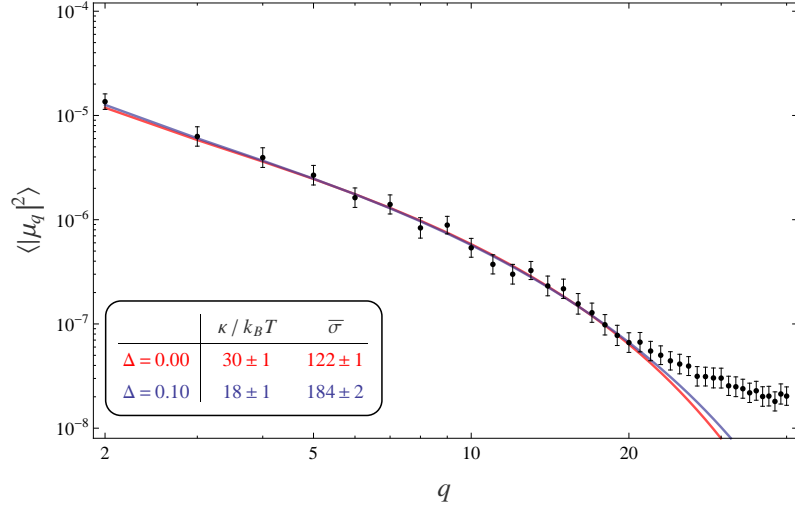


Figure S.4. Fluctuation spectrum for a GUV ($R \approx 8.9 \mu\text{m}$) imaged via phase contrast microscopy, with $\Delta = 0.10$ and $\tau \approx 4$ ms, on a log-log scale. Lines are the best-fit for the “standard” model (*i.e.* incorrectly assuming $\Delta = 0$, red), and for our model with $\Delta = 0.10$ (blue). Both fits are of similar quality, but their best-fit values are significantly different, see the inset table (same colors). In this experiment, we use $q_{\min} = 3$; the q -cutoffs are found to be $q_c = 13$ and $q_w = 28$, therefore we fixed $q_{\max} = 20$.

temperature characteristic of the experiment. The theoretical background of these fitting routines is fully detailed in the “Data analysis” section of this document.

Application to non-confocal imaging

In this subsection we report a proof of concept example of the use of our method to analyse a non-confocal “flickering” experiment. In this example, we use our routines to analyse a video acquired using the same microscope used for the confocal microscopy experiments, used now in Phase Contrast imaging mode. For this phase-contrast experiment, we used a Nikon Hcx PL Fluotar L 40X objective, operating in air, with numerical aperture $\text{NA} = 0.6$. We estimate the focal depth to be $2\mu\text{m}$ in these conditions, a value compatible with the output of the standard formula $d = \frac{\lambda}{\text{NA}^2}$. The fitting was performed using $q_{\min} = 3$, as in the confocal experiment. Since the q -cutoffs are found to be $q_c = 13$ and $q_w = 28$, we set fitting limit $q_{\max} = 20$. Results are reported in Fig. S.4. As shown by the inset, our method applied to phase contrast experiments still yields a value of $\kappa = 18k_B T$ which is in agreement with the literature values for DOPC.

S.2 Theoretical Model

Quasi-spherical vesicles

The usual theoretical description of GUVs is treated within a quasi-spherical approximation, where the membrane surface, say \mathcal{S} , is parametrised by the spherical angular coordinates (θ, φ) , with the surface

positional vector given by

$$\mathbf{R}(\theta, \varphi) = R[1 + u(\theta, \varphi)] \hat{\mathbf{r}}(\theta, \varphi), \quad (\text{S.2.1})$$

where $u(\theta, \varphi)$ is a local deviation about a reference sphere of radius R in a Monge-type representation, and $\hat{\mathbf{r}}(\theta, \varphi)$ is the radial unit vector normal to this sphere. The volume V_0 enclosed by the membrane of GUVs is considered to be constant, which in turn defines $R := (3V_0/4\pi)^{1/3}$.

Furthermore, the fluctuations about the reference sphere are assumed to be small and slowly varying (that is, the magnitude $|u(\theta, \varphi)| \ll 1$ and the gradient $|\nabla u(\theta, \varphi)| \ll 1$), so that the free-energy \mathcal{F} , see equation (2) in the Letter, can be written as a quadratic expansion in $u(\theta, \varphi)$. To obtain this expansion, we follow the works of [8] and [9], where the area of the vesicle $\mathcal{A} := \int_{\mathcal{S}} dS$, its volume $V := \frac{1}{3} \int_{\mathcal{S}} dS (\hat{\mathbf{n}} \cdot \mathbf{R})$, with $\hat{\mathbf{n}}$ as its surface normal, the integrated mean-curvature term $\mathcal{Q}_1 := \int_{\mathcal{S}} dS H$, and also the bending term $\mathcal{Q}_2 := \int_{\mathcal{S}} dS H^2$ can be approximated by a second-order Taylor expansion in u as follows:

$$\mathcal{A} = 4\pi R^2 - R^2 \int_0^\pi \int_0^{2\pi} \left[2u + u^2 + \frac{1}{2} (\nabla u)^2 \right] \sin(\theta) d\theta d\varphi, \quad (\text{S.2.2})$$

$$V = V_0 + R^3 \int_0^\pi \int_0^{2\pi} (u + u^2) \sin(\theta) d\theta d\varphi, \quad (\text{S.2.3})$$

$$\mathcal{Q}_1 = 4\pi R + R \int_0^\pi \int_0^{2\pi} \left[u + \frac{1}{2} (\nabla u)^2 - \frac{1}{2} (\nabla^2 u) \right] \sin(\theta) d\theta d\varphi, \quad (\text{S.2.4})$$

and

$$\mathcal{Q}_2 = 4\pi + \int_0^\pi \int_0^{2\pi} \left[u (\nabla^2 u) - (\nabla^2 u) + \frac{1}{2} (\nabla u)^2 + \frac{1}{4} (\nabla^2 u)^2 \right] \sin(\theta) d\theta d\varphi, \quad (\text{S.2.5})$$

respectively, where the differential operators ∇ and ∇^2 are defined with respect to the metric of a unit sphere, that is,

$$\nabla := \mathbf{e}_\theta \frac{\partial}{\partial \theta} + \frac{\mathbf{e}_\varphi}{\sin(\theta)} \frac{\partial}{\partial \varphi}, \quad \text{and} \quad \nabla^2 := \frac{1}{\sin(\theta)} \frac{\partial}{\partial \varphi} \left[\sin(\theta) \frac{\partial}{\partial \varphi} \right] + \frac{1}{\sin^2(\theta)} \frac{\partial^2}{\partial \theta^2}, \quad (\text{S.2.6})$$

with \mathbf{e}_θ and \mathbf{e}_φ as the unit vectors associated to the spherical angular coordinates.

Therefore, by ignoring the Gaussian curvature term in \mathcal{F} due to the constrained topology of GUVs, the effective free-energy of the fluid membrane \mathcal{S} is given by $\mathcal{F} = \mathcal{C}_0 \mathcal{A} + \mathcal{C}_1 \mathcal{Q}_1 + \mathcal{C}_2 \mathcal{Q}_2$, where \mathcal{C}_0 , \mathcal{C}_1 , and \mathcal{C}_2 are defined by

$$\mathcal{C}_0 = \sigma + 2\kappa H_0^2, \quad \mathcal{C}_1 = -2\kappa H_0, \quad \text{and} \quad \mathcal{C}_2 = 2\kappa, \quad (\text{S.2.7})$$

where σ is the surface tension, H_0 is the spontaneous curvature, and the curvature parameters κ is the bending modulus. Also, by expressing $u(\theta, \varphi)$ in the basis of spherical harmonics Y_n^m [10]:

$$u(\theta, \varphi) = \sum_{n=0}^{n_\infty} \sum_{m=-n}^n \mathcal{U}_{n,m} Y_n^m(\theta, \varphi), \quad (\text{S.2.8})$$

where $\mathcal{U}_{n,m}$ is the amplitude associated to each mode (n,m) and n_∞ is an ultraviolet cutoff¹, then the effective free-energy \mathcal{F} can be written in the following diagonalised form (a full derivation can be found in [9]):

$$\mathcal{F} = 4\pi\kappa(2 + \bar{\sigma}) + \frac{1}{2} \sum_{n=2}^{n_\infty} H(n) \sum_{m=-n}^n |\mathcal{U}_{n,m}|^2, \quad (\text{S.2.9})$$

where $|\mathcal{U}_{n,m}|$ is the complex modulus of the harmonic amplitude $\mathcal{U}_{n,m}$, the function $H(n)$ is defined by

$$H(n) = \kappa(n-1)(n+2) [\bar{\sigma} + n(n+1)], \quad (\text{S.2.10})$$

and $\bar{\sigma}$ is the reduced surface tension, namely

$$\bar{\sigma} = \frac{\sigma R^2}{\kappa} - 2H_0 R + 2H_0^2 R^2. \quad (\text{S.2.11})$$

The zeroth order coefficient $\mathcal{U}_{0,0}$ in equation (S.2.8) can be fixed by employing the constraint that the volume V of the GUVs remains unchanged under a small local deformation $u(\theta, \varphi)$, that is, $V = V_0$ in (S.2.3). This implies the following condition:

$$\mathcal{U}_{0,0} = -\frac{1}{\sqrt{4\pi}} \sum_{n=0}^{n_\infty} \sum_{m=-n}^n |\mathcal{U}_{n,m}|^2, \quad (\text{S.2.12})$$

which essentially corresponds to a rescaling of the frame radius [8]. Thus, its contribution to (S.2.9) can be omitted without loss of generality. It is noteworthy to mention that the three spherical harmonic modes given by $n = 1$ do not affect the area \mathcal{A} and the effective free-energy \mathcal{F} , as they correspond to pure translations of the vesicle, which incur no energetic cost since $H(n=1) = 0$. As a result, the sum in (S.2.9) can be restricted solely to modes $n \geq 2$ [9].

By introducing a fictitious external field in (S.2.9), as a *vector* $\mathbf{J} := \{\mathcal{J}_{n,m}\}$, that linearly couples to the amplitude vector $\mathbf{U} := \{\mathcal{U}_{n,m}\}$, where the integers $n \geq 2$ and $|m| \leq n$, then equation (S.2.9) can be concisely rewritten in terms of the following functional form:

$$\mathcal{F}[\mathbf{J}, \mathbf{U}] = 4\pi\kappa(2 + \bar{\sigma}) + \frac{1}{2} \mathbf{U}^\top \mathbf{H} \mathbf{U}^* - \mathbf{J}^\top \mathbf{U}, \quad (\text{S.2.13})$$

where \mathbf{H} is a diagonal *matrix* whose components are given by $H(n)$, and the symbols $*$ and \top denote a complex conjugate and a transpose, respectively. As a consequence, the thermodynamic properties of the model can be obtained from the partition function [11]:

$$\mathcal{Z}[\mathbf{J}] = \int \mathcal{D}\mathbf{U} \exp\left(-\frac{\mathcal{F}[\mathbf{J}, \mathbf{U}]}{k_B T}\right), \quad (\text{S.2.14})$$

where the integration measure $\mathcal{D}\mathbf{U} := \prod_{n=2}^{n_\infty} \{\prod_{m=0}^n d\Re[\mathcal{U}_{n,m}]\} \{\prod_{m=1}^n d\Im[\mathcal{U}_{n,m}]\}$, with $\Re[\mathcal{U}_{n,m}]$ and $\Im[\mathcal{U}_{n,m}]$ being the real and imaginary parts of $\mathcal{U}_{n,m}$. Due to the quadratic nature of (S.2.13), the partition

¹The upper mode cutoff $n_\infty \simeq R/\xi$, where ξ is on the order of the membrane thickness. Thus, using a typical radius of GUVs, say $R \sim 25 \mu\text{m}$, and a value of $\xi \sim 5 \text{ nm}$, then $n_\infty \sim 5 \times 10^3$.

function in (S.2.14) can be analytically computed, up to an unimportant prefactor, as follows [11]:

$$\mathcal{Z}[\mathbf{J}] \propto \exp\left(\frac{\mathbf{J}^T \mathbf{H}^{-1} \mathbf{J}^*}{2k_B T}\right), \quad (\text{S.2.15})$$

where \mathbf{H}^{-1} is the inverse matrix of \mathbf{H} . Hence, the thermodynamic average of the flickering amplitudes $\mathcal{U}_{n,m}$ and their correlation functions can be determined by using the derivatives of $\ln \mathcal{Z}$ with respect to the fictitious external fields $\mathcal{J}_{n,m}$ [11], namely

$$\langle \mathcal{U}_{n,m} \rangle = \frac{\partial}{\partial \mathcal{J}_{n,m}} \left(k_B T \ln \mathcal{Z}[\mathbf{J}] \right) \Big|_{\mathbf{J}=0} = 0 \quad (\text{S.2.16})$$

and

$$\langle \mathcal{U}_{n,m} \mathcal{U}_{k,\ell}^* \rangle = \frac{\partial^2}{\partial \mathcal{J}_{n,m} \partial \mathcal{J}_{k,\ell}^*} \left(k_B T \ln \mathcal{Z}[\mathbf{J}] \right) \Big|_{\mathbf{J}=0} = \frac{k_B T}{H(n)} \delta_{nk} \delta_{m\ell}, \quad (\text{S.2.17})$$

where δ_{nm} is the Kronecker delta function, which equals one if $n = m$ and vanishing otherwise. Hence, the equation (S.2.17) shows that the harmonic amplitudes are completely uncorrelated if the spherical modes $n \neq k$, and the mean-squared deviations $\langle |\mathcal{U}_{n,m}|^2 \rangle$ are independent of m and also a function of the membrane elastic constants, i.e. the bending modulus κ and the reduced surface tension $\bar{\sigma}$. Thus, they can be measured if the local variations in the three-dimensional shape of the GUVs can be observed and recorded over a sufficiently long time span.

Projection of surface fluctuations

A lipid vesicle observed using light microscopy yields only a two-dimensional projection of its membrane onto the focal plane of the microscope. Therefore, the contact between the experimentally measured contours (which are determined by an edge-detection algorithm) and the three-dimensional model of the membrane surface, as given by (S.2.17), has typically been established by focusing on the two-dimensional contours obtained through the intersection of the vesicle with the focal plane of the objective.

This cross-sectional plane is usually chosen to be at the equator of the lipid vesicle ($\theta = \pi/2$), where the diameter of the contours is found to be the largest, and also where the contrast is typically maximal². Thus, the radial position of the membrane in the equatorial plane of the vesicle, $\rho_0(\varphi, t) := \|\mathbf{R}(\theta = \pi/2, \varphi, t)\|$, can be used as an experimental observable, which now has an explicit time dependence. The time-average of the squared deviations in $\rho_0(\varphi, t)$ about the mean radius R can be related to (S.2.17) by assuming the ergodic hypothesis (namely, a long time-average of a macroscopic variable is equivalent to its thermal average [11]). In other words, the Fourier transform of the variations

²In the case of lipid vesicles which enclose a fluid that has the same density as the bulk solvent, the maximum contrast and the largest diameter of the contours are indeed found at $\theta = \pi/2$. However, the interior fluid is typically of a different density to ensure sedimentation of the vesicles to a substrate. In this case, the shape of vesicles is perturbed due to gravitational effects [12], which means that the position of the plane with the maximum diameter is no longer located at the equator of GUVs. However, such gravity effects are negligible if $\Delta\rho g R^4 \lesssim \kappa(12 + \bar{\sigma})$, as calculated in [12], where $g = 9.81 \text{ m/s}^2$ and $\Delta\rho$ is the density difference between the inside and the outside of the vesicle. Typically, this condition is readily satisfied in flicker spectroscopy experiments [6] and thus the gravitational effects are ignored throughout this study.

in $\rho_0(\varphi, t)$ about its mean value, that is,

$$u_q(t) := \frac{1}{2\pi} \int_{-\pi}^{+\pi} d\varphi e^{-iq\varphi} u\left(\theta = \frac{\pi}{2}, \varphi\right), \quad (\text{S.2.18})$$

which is non-dimensionalised by R , can be used to obtain a fluctuation spectrum in terms of the integer Fourier modes q , which is defined by the following autocorrelation function:

$$\langle u_q(t) u_q^*(t) \rangle_t = \sum_{n \geq q} \mathcal{E}_{n,q}^2 \langle |\mathcal{U}_{n,q}|^2 \rangle, \quad (\text{S.2.19})$$

where the coefficients $\mathcal{E}_{n,q} = Y_n^q(\theta = \pi/2, \varphi = 0)$, and $\langle \cdot \rangle_t$ denotes a time-average over the total duration of the experiment (which is identical to the thermal average as the system is assumed to be ergodic). The result in (S.2.19) can be derived by employing the equations (S.2.8) and (S.2.17), together with the orthogonality of the spherical harmonic functions Y_n^m , and the double summation identity $\sum_{k=0}^{\infty} \sum_{k=-\ell}^{+\ell} \mathcal{B}_{k,\ell} = \sum_{\ell=-\infty}^{\infty} \sum_{k=\ell}^{\infty} \mathcal{B}_{k,\ell}$.

Another experimental issue, which further complicates the comparison of the experimental data with the fluctuation spectrum (S.2.19), is that the observed two-dimensional contours are, in practice, averaged over the integration time τ of the microscope. This introduces an experimental limitation that results in significant averaging effects of the shape fluctuations when their characteristic life-times are shorter than the acquisition time of the microscope. Hence, its consequences on the fluctuation spectrum have been widely studied [6]. To quantitatively account for this averaging, the relaxation times τ_n associated to each spherical harmonic mode needs to be adequately determined. By using a simple viscoelastic theory of a spherical vesicle, as derived in [9], we find that $\mathcal{U}_{n,m}(t) = \mathcal{U}_{n,m}(0) e^{-t/\tau_n}$, where the mono-exponential decay time of each mode are found to be

$$\tau_n = \frac{R^3}{H(n)} \left[\eta_{\text{in}} \frac{(n+2)(2n-1)}{n+1} + \eta_{\text{out}} \frac{(n-1)(2n+3)}{n} \right], \quad (\text{S.2.20})$$

with η_{in} and η_{out} as the viscosities of the surrounding fluid found in the inside and the outside of the vesicle, respectively. As a result, due to the finite acquisition time τ of the microscope (which is usually on the order of microseconds), the time correlation function of the equatorial fluctuations in (S.2.19) becomes [9]:

$$\langle \bar{u}_q(t) \bar{u}_q^*(t) \rangle_t = \sum_{n \geq q} \mathcal{E}_{n,q}^2 \langle |\mathcal{U}_{n,q}|^2 \rangle \frac{\tau_n^2}{\tau^2} \left(1 - e^{-\tau/\tau_n} \right)^2, \quad (\text{S.2.21})$$

where we define $\bar{u}_q(t) := \tau^{-1} \int_0^\tau dt' u_q(t+t')$. Thus, the methodology involves relating (S.2.21) to the spectrum computed from the experimentally observed contours, which allows us to estimate the membrane bending modulus and its surface tension.

Although this approach of projecting the fluctuations onto the equatorial plane may appear to be a reasonable approximation, we maintain that the equatorial plane of the GUVs is not what is actually observed under an optical microscope. Strictly speaking, the equator of the vesicle contains a vanishing area in projection, and it is therefore invisible to the usual video-microscopy techniques. Thus, we assume that what is observed is a projection over a strip of membrane material within a small region in

the vicinity of the equator. This strip can support a spectrum of surface modes, which are averaged out in projection.

Measured intensity from quasi-spherical vesicles

To examine the effect due to the projection of the shape undulations onto the focal plane of the microscope, we need to understand how the averaging of fluctuations out of this plane affects the light intensity entering the camera. However, since the latter usually depends on the specific imaging technique used in the experiments and various other optical considerations, the full analysis is a highly non-trivial task. Here, we introduce an approach, which allows us to construct an intensity field that mimics closely some of the features of its experimental counterpart.

Firstly, we consider that light arriving from a point on the membrane surface that is located at a height z above, or below, the focal plane (or equivalently, the equatorial plane of the vesicle) has an intensity which is scaled by a Gaussian kernel $\mathcal{G}(z)$, namely

$$\mathcal{G}(z) = \exp \left[-\frac{1}{2\Delta^2} \left(\frac{z}{R} \right)^2 \right], \quad (\text{S.2.22})$$

where R is the mean radius of the vesicle, and Δ is a dimensionless parameter that characterises the focal depth of the microscope.

Secondly, we assume that the vesicle radiates light isotropically (e.g. its membrane is uniformly fluorescent), and furthermore there is no refraction or absorption, which implies that the infinitesimal radiant power $d\mathfrak{A}$ emanated by a small membrane patch $d\mathcal{A}$ is given by $d\mathfrak{A} = \hat{\mathcal{I}}_0 d\mathcal{A}$, where $\hat{\mathcal{I}}_0$ is the intensity detected at $z = 0$. As a result, the observed intensity field in the focal plane, say $\hat{\mathcal{I}}(r, \varphi)$, is proportional to the projected mass density of membrane, since $d\mathfrak{A} = \mathcal{I}_0 d\mathcal{A} = \hat{\mathcal{I}}(r, \varphi) d\mathcal{A}_p$, where \mathcal{A}_p is the surface element given by the projection of the membrane patch $d\mathcal{A}$ onto the focal plane. This means that $\hat{\mathcal{I}}(r, \varphi)$ is purely a geometrical object that only depends on the three-dimensional configuration of the vesicle.

By taking into account the Gaussian scaling in (S.2.22), we can construct an intensity field of the light entering the camera, analogous to $\hat{\mathcal{I}}(r, \varphi)$, as follows:

$$\begin{aligned} \mathcal{I}(r, \varphi) \propto \iiint d\Omega \mathcal{G}(r' \cos \theta') \delta(r - r' \sin \theta') \\ \delta(r' \varphi' \sin \theta' - r\varphi) \delta(r' - \|\mathbf{R}(\theta', \varphi')\|), \end{aligned} \quad (\text{S.2.23})$$

where the volume integral $\iiint d\Omega := \int_0^\infty dr' r'^2 \int_0^\pi d\theta' \sin \theta' \int_0^{2\pi} d\varphi'$, δ represents a Dirac delta function, and the position vector $\mathbf{R}(\theta', \varphi')$ is defined by (S.2.1). Here, r' measures the radial distance from the centre of the vesicle, and (θ', φ') are the usual spherical angular coordinates, with $\theta' = 0$ (or π) indicating the normal direction of a point above (or below) the focal plane of the objective. On the other hand, the variables r and φ are the polar coordinates in the equatorial plane, with the origin chosen to be at the centre of the vesicle. Moreover, the first delta function in (S.2.23) gives the projection of radial distances onto the focal plane, the second one specifies that the azimuthal angles are equivalent in both three-

dimensional and two-dimensional reference frames, and the third one is a constraint that locates the position of the membrane surface relative to the centre of the vesicle. Thus, by using a quasi-spherical representation, the volume integral over these Dirac delta functions yields the projected shape of the vesicle for a given realisation of the local field $u(\theta', \varphi')$.

Lowest-order radial moment

The simplest way of extracting information from (S.2.23) is to analyze the first radial moment of the intensity field,

$$\rho_{\Delta}(\varphi) = \frac{\int_0^{\infty} r \mathcal{I}(r, \varphi) dr}{\int_0^{\infty} \mathcal{I}(r, \varphi) dr}. \quad (\text{S.2.24})$$

Reassuringly, this object recovers in the limit of $\Delta \rightarrow 0$ (see equation (S.2.37) later in this section) the experimental observable $\rho_0(\varphi)$, namely the radial position of the membrane in the equatorial plane of the vesicle. By integrating over the angular variables θ' and φ' in (S.2.23), the intensity field $\mathcal{I}(r, \varphi)$ can be reduced to a single integral, that is,

$$\mathcal{I} \propto \int_r^{\infty} dr' \frac{\mathcal{G}(r' \cos \Theta)}{R \cos \Theta} \left\{ \delta \left[\frac{r'}{R} - 1 - u(\Theta, \varphi) \right] + \delta \left[\frac{r'}{R} - 1 - u(\pi - \Theta, \varphi) \right] \right\}, \quad (\text{S.2.25})$$

where $\Theta = \arcsin(r/r')$ is introduced as a shorthand notation for the sake of clarity. Hence, using the substitutions $r = \xi R$ and $r' = \xi R \cosh(\psi)$ in the equation (S.2.25), then the expression of the first moment (S.2.24) is given by

$$\rho_{\Delta}(\varphi) = \frac{R \int_0^{\infty} \xi d\xi \int_0^{\infty} d\psi \xi \cosh(\psi) [\mathfrak{D}(\psi, \xi, \Theta) + \mathfrak{D}(\psi, \xi, \pi - \Theta)] e^{-\frac{\xi^2 \sinh^2 \psi}{2\Delta^2}}}{\int_0^{\infty} d\xi \int_0^{\infty} d\psi \xi \cosh(\psi) [\mathfrak{D}(\psi, \xi, \Theta) + \mathfrak{D}(\psi, \xi, \pi - \Theta)] e^{-\frac{\xi^2 \sinh^2 \psi}{2\Delta^2}}}, \quad (\text{S.2.26})$$

where the function \mathfrak{D} is defined by

$$\mathfrak{D}(\psi, \xi, \hat{\Theta}) := \delta [\xi \cosh \psi - 1 - u(\hat{\Theta}, \varphi)]. \quad (\text{S.2.27})$$

Moreover, the delta functions in (S.2.26) can be eliminated by changing the order of integration and then evaluating the integrals over the variable ξ , which yields

$$\mu(\varphi) = \frac{\int_0^1 d\omega (1 + u_N)^2 \exp\left(-\frac{(1+u_N)^2}{2\Delta^2} \omega^2\right) + (1 + u_S)^2 \exp\left(-\frac{(1+u_S)^2}{2\Delta^2} \omega^2\right)}{\int_0^1 d\omega \frac{(1+u_N)}{\sqrt{1-\omega^2}} \exp\left(-\frac{(1+u_N)^2}{2\Delta^2} \omega^2\right) + \frac{(1+u_S)}{\sqrt{1-\omega^2}} \exp\left(-\frac{(1+u_S)^2}{2\Delta^2} \omega^2\right)}, \quad (\text{S.2.28})$$

where we define $\mu(\varphi) := \rho_{\Delta}(\varphi)/R$, $u_N := u(\Theta, \varphi)$ and $u_S := u(\pi - \Theta, \varphi)$, and a change of variables $\omega = \tanh(\psi)$ is used to further simplify the expression.

Since the shape undulations are assumed to be small compared to the mean radius of the quasi-sphere, namely $|u| \ll 1$, the equation (S.2.28) can be expanded to first order in u_N and u_S , and found to be a function of only $\tilde{u} := u_N + u_S$, as follows:

$$\mu(\varphi) = \mu_0 + \frac{\int_0^1 d\omega \left(\frac{2\Delta^2 + \omega^2}{\Delta^2} - \mu_0 \frac{\Delta^2 + \omega^2}{\Delta^2 \sqrt{1-\omega^2}} \right) \tilde{u}(\omega, \varphi) e^{-\frac{\omega^2}{2\Delta^2}}}{2 \int_0^1 \frac{d\omega}{\sqrt{1-\omega^2}} e^{-\frac{\omega^2}{2\Delta^2}}} + \mathcal{O}(\tilde{u}^2), \quad (\text{S.2.29})$$

where the coefficient μ_0 is the zeroth order term in the expansion of $\mu(\varphi)$, which is given by

$$\mu_0 = \frac{\int_0^1 d\omega e^{-\frac{\omega^2}{2\Delta^2}}}{\int_0^1 \frac{d\omega}{\sqrt{1-\omega^2}} e^{-\frac{\omega^2}{2\Delta^2}}} = \frac{\frac{\Delta\sqrt{\pi}}{\sqrt{2}} \operatorname{erf}\left(\frac{1}{\Delta\sqrt{2}}\right)}{\frac{\pi}{2} I_0\left(\frac{1}{4\Delta^2}\right) e^{-\frac{1}{4\Delta^2}}} \stackrel{\Delta \rightarrow 0}{=} 1, \quad (\text{S.2.30})$$

with erf as the error function and I_0 as the modified Bessel function of the first kind of order zero [10]. Thus, equation (S.2.29) gives the first order perturbation about the spherical configuration, $\hat{\mu}(\varphi) := \mu(\varphi) - \mu_0$, namely

$$\hat{\mu}(\varphi) = \frac{\exp\left(\frac{1}{4\Delta^2}\right)}{\pi I_0\left(\frac{1}{4\Delta^2}\right)} \int_0^1 d\omega \left(\frac{2\Delta^2 + \omega^2}{\Delta^2} - \mu_0 \frac{\Delta^2 + \omega^2}{\Delta^2 \sqrt{1-\omega^2}} \right) \tilde{u}(\omega, \varphi) e^{-\frac{\omega^2}{2\Delta^2}}. \quad (\text{S.2.31})$$

Analogous to the calculation of the equatorial fluctuations, this azimuthal function can now be used to obtain a fluctuation spectrum by Fourier transforming it in the angle φ , yielding $\hat{\mu}_q$, and subsequently by computing the thermal ensemble average of $|\hat{\mu}_q|^2$. By Fourier transforming equation (S.2.31) with respect to the angle φ , this yields

$$\hat{\mu}_q := \frac{1}{2\pi} \int_{-\pi}^{+\pi} d\varphi \hat{\mu}(\varphi) e^{iq\varphi} = \int_0^1 d\omega \mathcal{N}(\omega, \Delta) \tilde{u}_q(\omega), \quad (\text{S.2.32})$$

where in the last step we use the explicit form of (S.2.31) and then interchange the order of integration. Hence, by defining the Fourier transform of $\tilde{u}(\omega, \varphi)$ as $\tilde{u}_q(\omega)$, and also by absorbing the other remaining terms in $\mathcal{N}(\omega, \Delta)$, then the final result in equation (S.2.32) can be obtained.

By using the basis representation in (S.2.8) and by rewriting the spherical harmonic functions as $Y_n^m(\theta, \varphi) = e^{im\varphi} \mathcal{P}_n^m(\cos\theta)$, where

$$\mathcal{P}_n^m(\cos\theta') = \sqrt{\frac{2n+1}{4\pi} \frac{(n-m)!}{(n+m)!}} P_n^m(\cos\theta'), \quad (\text{S.2.33})$$

with P_n^m being the associated Legendre polynomials [10], then the Fourier transform of $\tilde{u}(\omega, \varphi)$ is found to be

$$\tilde{u}_q(\omega) = \sum_{n \geq q} \mathcal{U}_{n,q} [\mathcal{P}_n^q(\omega) + \mathcal{P}_n^q(-\omega)] = \sum_{n \geq q} \mathcal{U}_{n,q} \mathcal{P}_n^q(\omega) [1 + (-1)^{n+q}], \quad (\text{S.2.34})$$

where the identity $\mathcal{P}_n^q(-\omega) = (-1)^{n+q} \mathcal{P}_n^q(\omega)$ is used in the last step [10]. As a result, using (S.2.32),

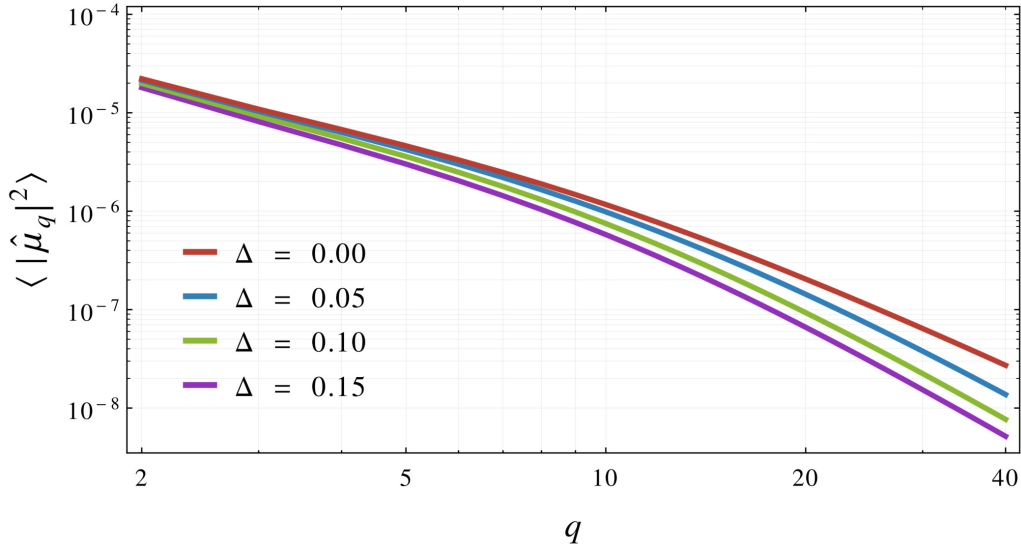


Figure S.5. Log-log plot of the mean squared amplitudes $\langle |\hat{\mu}_q|^2 \rangle$ as a function of the azimuthal mode number q for some values of the focal depth Δ . Here, $\kappa = 20 k_B T$ and $\bar{\sigma} = 100$, and a straight line interpolation is used between the points.

the mean squared amplitude of each Fourier mode can be determined as follows (see Figure S.5):

$$\langle |\hat{\mu}_q|^2 \rangle = \sum_{n \geq q} \langle |\mathcal{U}_{n,q}|^2 \rangle \left\{ [1 + (-1)^{n+q}] \int_0^1 d\omega \mathcal{N}(\omega, \Delta) \mathcal{P}_n^q(\omega) \right\}^2, \quad (\text{S.2.35})$$

where the orthogonality of the flickering amplitudes in (S.2.17) is employed. Moreover, using the explicit form of $\mathcal{N}(\omega, \Delta)$, the term in the curly brackets, say $\mathcal{L}_{n,q}$, can be written as

$$\mathcal{L}_{n,q} = \frac{1 + (-1)^{n+q}}{\pi I_0 \left(\frac{1}{4\Delta^2} \right) e^{-\frac{1}{4\Delta^2}}} \int_0^1 d\omega \mathcal{P}_n^q(\omega) \left[\frac{2\Delta^2 + \omega^2}{\Delta^2} - \frac{\mu_0 (\Delta^2 + \omega^2)}{\Delta^2 \sqrt{1 - \omega^2}} \right] e^{-\frac{\omega^2}{2\Delta^2}}, \quad (\text{S.2.36})$$

which recovers the coefficients $\mathcal{E}_{n,q}$ of (S.2.19) in the limit of $\Delta \rightarrow 0$ as expected. This can be shown by a method of steepest descent. Namely, when Δ goes to zero, the exponential term within the integrand of (S.2.36) vanishes unless $\omega = 0$. Therefore, the term in the square brackets of (S.2.36) tends to unity, and the integral reduces to

$$\lim_{\Delta \rightarrow 0} \mathcal{L}_{n,q} = \lim_{\Delta \rightarrow 0} \frac{1 + (-1)^{n+q}}{\pi I_0 \left(\frac{1}{4\Delta^2} \right) e^{-\frac{1}{4\Delta^2}}} \int_0^1 d\omega \mathcal{P}_n^q(0) e^{-\frac{\omega^2}{2\Delta^2}} = \lim_{\Delta \rightarrow 0} \frac{\mu_0}{2} [1 + (-1)^{n+q}] \mathcal{P}_n^q(0), \quad (\text{S.2.37})$$

which leads to $\mathcal{E}_{n,q}$ by using (S.2.33), (S.2.30), and the property that $\mathcal{P}_n^m(0) = 0$ when $n + m$ is an odd integer number [10]. Although it is possible to find a closed form expression for $\mathcal{L}_{n,q}$ by performing the integral exactly, the general result involves two finite sums over four confluent hypergeometric functions of the first kind [10], and thus it is not any more enlightening than the result given by (S.2.36). However, this means that on a practical level $\mathcal{L}_{n,q}$ can be tabulated for some fixed n and q , instead of numerically evaluating the integral (see LTable.nb and Table S.1).

(n, q)	$\mathcal{L}_{n,q}$
(2, 2)	$\frac{e^{-\frac{1}{4\Delta^2}} \left\{ 10\sqrt{30}\Delta^2 I_0\left(\frac{1}{4\Delta^2}\right) - \sqrt{15\pi} e^{2\Delta^2} \Delta \left[5(2\Delta^2 - 1) I_0\left(\frac{1}{4\Delta^2}\right) + 3I_1\left(\frac{1}{4\Delta^2}\right) \right] \operatorname{erf}\left(\frac{1}{\sqrt{2}\Delta}\right) \right\}}{8\pi^{3/2} \left[I_0\left(\frac{1}{4\Delta^2}\right) \right]^2}$
(4, 2)	$\frac{e^{-\frac{1}{4\Delta^2}} \left\{ 9\sqrt{10}\Delta^2 (49\Delta^2 + 3) I_0\left(\frac{1}{4\Delta^2}\right) - 3\sqrt{5\pi} e^{2\Delta^2} \Delta \left[(35\Delta^2 + 2) I_1\left(\frac{1}{4\Delta^2}\right) + (147\Delta^4 - 40\Delta^2 - 1) I_0\left(\frac{1}{4\Delta^2}\right) \right] \operatorname{erf}\left(\frac{1}{\sqrt{2}\Delta}\right) \right\}}{8\pi^{3/2} \left[I_0\left(\frac{1}{4\Delta^2}\right) \right]^2}$
(4, 4)	$\frac{e^{-\frac{1}{4\Delta^2}} \left\{ 9\sqrt{70} (1 - 7\Delta^2) \Delta^2 I_0\left(\frac{1}{4\Delta^2}\right) + 3\sqrt{35\pi} e^{2\Delta^2} \Delta \left[(5\Delta^2 - 1) I_1\left(\frac{1}{4\Delta^2}\right) + (21\Delta^4 - 10\Delta^2 + 2) I_0\left(\frac{1}{4\Delta^2}\right) \right] \operatorname{erf}\left(\frac{1}{\sqrt{2}\Delta}\right) \right\}}{16\pi^{3/2} \left[I_0\left(\frac{1}{4\Delta^2}\right) \right]^2}$
(6, 2)	$\frac{\sqrt{1365} e^{-\frac{1}{4\Delta^2}} \Delta \left\{ 4\Delta (4455\Delta^4 + 414\Delta^2 + 35) I_0\left(\frac{1}{4\Delta^2}\right) + \sqrt{2\pi} e^{2\Delta^2} \left[(-8910\Delta^6 + 2142\Delta^4 + 41\Delta^2 + 20) I_0\left(\frac{1}{4\Delta^2}\right) - 3(616\Delta^4 + 39\Delta^2 + 6) I_1\left(\frac{1}{4\Delta^2}\right) \right] \operatorname{erf}\left(\frac{1}{\sqrt{2}\Delta}\right) \right\}}{128\pi^{3/2} \left[I_0\left(\frac{1}{4\Delta^2}\right) \right]^2}$
(6, 4)	$\frac{3\sqrt{91} e^{-\frac{1}{4\Delta^2}} \Delta \left\{ \sqrt{\pi} e^{2\Delta^2} \left[(616\Delta^4 - 21\Delta^2 + 2) I_1\left(\frac{1}{4\Delta^2}\right) + (2970\Delta^6 - 966\Delta^4 + 53\Delta^2 - 4) I_0\left(\frac{1}{4\Delta^2}\right) \right] \operatorname{erf}\left(\frac{1}{\sqrt{2}\Delta}\right) - 6\sqrt{2} (495\Delta^5 + 4\Delta^3 + \Delta) I_0\left(\frac{1}{4\Delta^2}\right) \right\}}{64\pi^{3/2} \left[I_0\left(\frac{1}{4\Delta^2}\right) \right]^2}$
(6, 6)	$\frac{\sqrt{3003} e^{-\frac{1}{4\Delta^2}} \Delta \left\{ 12(45\Delta^5 - 6\Delta^3 + \Delta) I_0\left(\frac{1}{4\Delta^2}\right) + \sqrt{2\pi} e^{2\Delta^2} \left[(-56\Delta^4 + 11\Delta^2 - 2) I_1\left(\frac{1}{4\Delta^2}\right) + (-270\Delta^6 + 126\Delta^4 - 23\Delta^2 + 4) I_0\left(\frac{1}{4\Delta^2}\right) \right] \operatorname{erf}\left(\frac{1}{\sqrt{2}\Delta}\right) \right\}}{128\pi^{3/2} \left[I_0\left(\frac{1}{4\Delta^2}\right) \right]^2}$

Table S.1. The closed form expressions of the functions $\mathcal{L}_{n,q}$ for a few values of n and q . Here, the functions I_0 and I_1 are the modified Bessel functions of the first kind of order zero and one, respectively, and erf is the error function. In general, we have that $\mathcal{L}_{n,q} = 0$ if $n < q$ and also if $n + q$ is an odd integer number. A larger table of $\mathcal{L}_{n,q}$ can be found in [LTable.nb](#) file of the Supplemental Material.

The existing approach to determine the bending modulus in flicker spectroscopy experiments involves relating the time correlation function of the equatorial fluctuations, as given (S.2.21), to the fluctuation spectrum measured from the observed contours [6]. Analogous to the spectrum in equation (S.2.21), we can construct a time correlation function for the fluctuations in the first radial moment of the intensity field (S.2.23), namely

$$\langle \bar{\mu}_q(t) \bar{\mu}_q^*(t) \rangle_t = \sum_{n \geq q} \mathcal{L}_{n,q}^2 \langle |\mathcal{U}_{n,q}|^2 \rangle \frac{\tau_n^2}{\tau^2} \left(1 - e^{-\tau/\tau_n}\right)^2, \quad (\text{S.2.38})$$

where the time-average $\bar{\mu}_q(t) := \tau^{-1} \int_0^\tau dt' \hat{\mu}_q(t+t')$, τ is the acquisition time of the microscope, τ_q is the characteristic relaxation time associated to each spherical harmonic mode, as given by (S.2.20), and the functions $\mathcal{L}_{n,q}$ and $\langle |\mathcal{U}_{n,q}|^2 \rangle$ are defined by (S.2.36) and (S.2.17), respectively.

S.3 Data analysis

The best-fit parameters to the experimental data are found by means of a maximum likelihood estimate [13] for the model in Eq. (S.2.38), namely we seek to minimise the following function:

$$\chi_\Delta^2 = \sum_{q=q_{\min}}^{q_{\max}} \left[\frac{F_q(\Delta) - \langle \bar{\mu}_q(t) \bar{\mu}_q^*(t) \rangle_t}{\Sigma_q(\Delta)} \right]^2, \quad (\text{S.3.1})$$

where $\Sigma_q(\Delta)$ is the standard error in the mean associated to each $F_q(\Delta)$ measured for a particular Δ (focal depth per R). This is an application of Bayes' theorem. Using the components of the vectors \mathbf{F}_Δ and \mathbf{X} to denote the measured spectrum $\{F_q(\Delta)\}$ and the parameters of interest (e.g. we have $\mathbf{X} = (\kappa, \bar{\sigma})$ for a single vesicle, or $\mathbf{X} = (\kappa, \bar{\sigma}_1, \bar{\sigma}_2, \bar{\sigma}_3)$ for three vesicles that have the same lipid composition but different surface tensions – see later), respectively, we can tersely write that the posterior probability

$$\mathbb{P}(\mathbf{X} | \mathbf{F}_\Delta, \mathbf{I}) \propto \mathbb{P}(\mathbf{F}_\Delta | \mathbf{X}, \mathbf{I}) \cdot \mathbb{P}(\mathbf{X} | \mathbf{I}), \quad (\text{S.3.2})$$

where \mathbf{I} denotes all the relevant background information [13]. The last term in Eq. (S.3.2) is the prior probability that indicates everything we know about \mathbf{X} before the analysis of the data \mathbf{F}_Δ . In order to reflect complete ignorance (unbiased knowledge) of the latter, this is commonly taken to be a uniform probability, namely we have $\mathbb{P}(\mathbf{X} | \mathbf{I}) = \text{constant}$ for all values of \mathbf{X} [13]. Using this uniform assignment, then Eq. (S.3.2) simply becomes $\mathbb{P}(\mathbf{X} | \mathbf{F}_\Delta, \mathbf{I}) \propto \mathbb{P}(\mathbf{F}_\Delta | \mathbf{X}, \mathbf{I})$. Thus, the best estimate of \mathbf{X} (say \mathbf{X}_0), which is given by the maximum of the posterior $\mathbb{P}(\mathbf{X} | \mathbf{F}_\Delta, \mathbf{I})$, is equivalent to the solution that gives the largest value for the likelihood probability of the measured data $\mathbb{P}(\mathbf{F}_\Delta | \mathbf{X}, \mathbf{I})$. If we assume that the spectral data \mathbf{F}_Δ are entirely independent, which is motivated by the uncorrelation of modes in Eq. (S.2.17), then the joint probability $\mathbb{P}(\mathbf{F}_\Delta | \mathbf{X}, \mathbf{I})$ can be written as a product of the probabilities for the individual measurements:

$$\mathbb{P}(\mathbf{F}_\Delta | \mathbf{X}, \mathbf{I}) = \prod_{q=q_{\min}}^{q_{\max}} \mathbb{P}(F_q(\Delta) | \mathbf{X}, \mathbf{I}) \quad (\text{S.3.3})$$

where q_{\min} and q_{\max} represent the lower and upper bound of the range in the measured spectrum used for the analysis. The choice of these bounds is discussed later in this section. If we also assume that the noise associated with the experimental measurements can be described by a Gaussian process, then the probability of an individual datum is given by

$$\mathbb{P}(F_q(\Delta) | \mathbf{X}, \mathbf{I}) = \frac{1}{\sqrt{2\pi}\Sigma_q} \exp \left\{ -\frac{[\langle \bar{\mu}_q(t) \bar{\mu}_q^*(t) \rangle_t - F_q(\Delta)]^2}{2\Sigma_q^2(\Delta)} \right\} \quad (\text{S.3.4})$$

where \mathbf{I} implicitly includes a knowledge of both the expected size of the uncertainties $\{\Sigma_q(\Delta)\}$, and a suitable model of the functional relationship between the parameters \mathbf{X} and the ideal (noiseless) data given by $\langle \bar{\mu}_q(t) \bar{\mu}_q^*(t) \rangle_t$ – see Eq. (S.2.38). As a result, the posterior for \mathbf{X} given the dataset \mathbf{F}_Δ is found to be

$$\mathbb{P}(\mathbf{X} | \mathbf{F}_\Delta, \mathbf{I}) \propto \exp \left(-\frac{\chi_\Delta^2}{2} \right) \prod_{q=q_{\min}}^{q_{\max}} \frac{1}{\sqrt{2\pi}\Sigma_q(\Delta)}, \quad (\text{S.3.5})$$

using Eqs. (S.3.1 – S.3.5). This shows that the maximum of the posterior occurs when χ_Δ^2 is smallest; the corresponding optimal solution \mathbf{X}_0 can be obtained by minimizing the weighted least-squares function (S.3.1) with respect to each parameter in \mathbf{X} .

To obtain a measure of reliability for the best estimate \mathbf{X}_0 , we need to study the spread of the posterior probability about the point \mathbf{X}_0 . Using a Taylor series expansion, the local behaviour of χ_Δ^2 takes the form (up to second-order):

$$\chi_\Delta^2 = \chi_{\min}^2 + \frac{1}{2} (\mathbf{X} - \mathbf{X}_0) \mathbf{H}_{\min} (\mathbf{X} - \mathbf{X}_0)^\top + \mathcal{O}[(\mathbf{X} - \mathbf{X}_0)^3], \quad (\text{S.3.6})$$

where $\chi_{\min}^2 = \chi_\Delta^2(\mathbf{X} = \mathbf{X}_0)$, and \mathbf{H}_{\min} is the Hessian matrix \mathbf{H} of (S.3.1) evaluated at the best-fit parameters [13]. This allows us to compute the covariance matrix \mathbf{C} of the posterior, which is formally defined to be the expectation value of the square-like deviations from the mean (that is, a multivariate case of the variance for a single variable), namely

$$[\mathbf{C}]_{ij} = \int \mathcal{D}\mathbf{X} (X_i - X_{0,i})(X_j - X_{0,j}) \mathbb{P}(\mathbf{X} | \mathbf{F}_\Delta, \mathbf{I}), \quad (\text{S.3.7})$$

where $\{X_j\}$ and $\{X_{0,j}\}$ are the associated components of the vectors \mathbf{X} and \mathbf{X}_0 , respectively, and the measure $\mathcal{D}\mathbf{X} := \prod_\ell dX_\ell$. The associated error-bar with respect to X_ℓ is therefore given by the square root of $[\mathbf{C}]_{\ell\ell}$. Using Eqs. (S.3.5) and (S.3.6), we find that $\mathbf{C} = -\mathbf{H}_{\min}^{-1}$ [13].

We return to the question of what values we should consider for q_{\min} and q_{\max} . This is yet again another application of Bayes' theorem (a model selection problem, see [13]). For simplicity, the lower bound of the fitting range is taken to be a constant throughout this study; specifically, we choose $q_{\min} = 3$, because the second mode can be affected by imaging artefacts, *e.g.* a slight asymmetry between the longitudinal and vertical pixel size. The optimal choice for the upper bound is one that maximises its posterior probability in the view of the dataset \mathbf{F}_Δ . Using the Bayes' theorem and the usual rules of

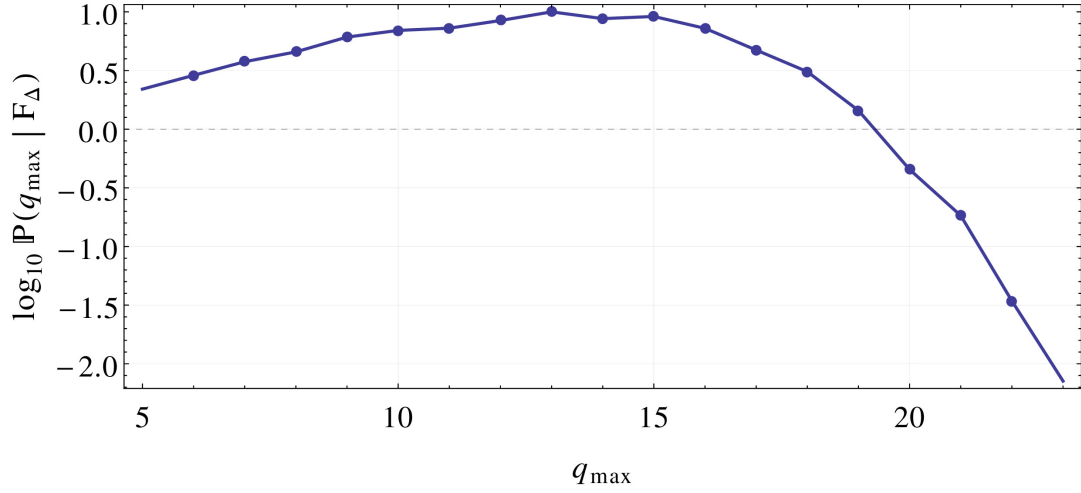


Figure S.6. The logarithm of the posterior probability for the upper bound q_{\max} given the data (namely, the spectrum shown in Figure 2 of the Letter), which is scaled by its maximum (here, the optimal value is given by $q_{\max} = 13$). A straight line interpolation is used between the points.

probability theory [13], it can be shown that

$$\mathbb{P}(q_{\max} | \mathbf{F}_{\Delta}, \mathbf{I}) \propto \int \mathcal{D}\mathbf{X} \mathbb{P}(\mathbf{X} | \mathbf{F}_{\Delta}, \mathbf{I}) \quad (\text{S.3.8})$$

where the prior probabilities are assumed to be uniform, and all terms independent of q_{\max} are absorbed into the (omitted) normalisation constant of Eq. (S.3.8). For measurements on a single vesicle, the posterior probability in Eq. (S.3.8), together with Eq. (S.3.5), yields

$$\mathbb{P}(q_{\max} | \mathbf{F}_{\Delta}, \mathbf{I}) \propto \iint d\kappa d\bar{\sigma} \exp\left[-\frac{1}{2} \chi_{\Delta}^2(\kappa, \bar{\sigma})\right] \prod_{q=q_{\min}}^{q_{\max}} \frac{1}{\sqrt{2\pi}\Sigma_q}, \quad (\text{S.3.9})$$

since we simply have $\mathbf{X} = (\kappa, \bar{\sigma})$. Here, this double integral can be carried out numerically over some adequately chosen domain of integration. Alternatively, we can make further analytical progress by assuming that the form of χ_{Δ}^2 can be reasonably approximated by the second-order expansion about the optimal estimate $\mathbf{X}_0 = (\kappa_0, \bar{\sigma}_0)$, as given in Eq. (S.3.6). Consequently, the integral over $\exp(-\chi_{\Delta}^2/2)$ equals to the value of $\exp(-\chi_{\min}^2/2)$ times the integral over a two-dimensional Gaussian:

$$\iint d\kappa d\bar{\sigma} \exp\left[-\frac{1}{4} \begin{pmatrix} \kappa - \kappa_0 \\ \bar{\sigma} - \bar{\sigma}_0 \end{pmatrix} \mathbf{H}_{\min} \begin{pmatrix} \kappa - \kappa_0 \\ \bar{\sigma} - \bar{\sigma}_0 \end{pmatrix}\right] = \frac{4\pi}{\sqrt{\det(\mathbf{H}_{\min})}}, \quad (\text{S.3.10})$$

where $\det(\mathbf{H}_{\min})$ is the determinant of the Hessian matrix evaluated at $\mathbf{X}_0 = (\kappa_0, \bar{\sigma}_0)$.

This analytical result is used to select the optimal value of q_{\max} (see Fig. S.6). In addition, we impose that q_{\max} needs to be greater than the value of the crossover mode $q_c = R/\xi = \sqrt{\bar{\sigma}}$, where $\xi = \sqrt{\kappa/\bar{\sigma}}$ is the membrane correlation length, and the final equality holds as the mean spontaneous curvature $H_0 = 0$ in our experiments. This crossover mode separates the regimes in which the membrane

is mainly dominated by the surface tension term (when $q \lesssim q_c$) and the bending rigidity term (when $q \gtrsim q_c$). Since the fluctuation spectrum in these limits is characterised by different functional forms (e.g. in the usual Monge-like case [6], we find the power-laws q^{-2} and q^{-4} if the modes $q \lesssim q_c$ and $q \gtrsim q_c$, respectively), this crossover is required to lie within the fitting range, leading therefore to the condition that $q_{\min} < q_c < q_{\max}$. At the same time, the value of q_{\max} must be smaller than the cutoffs related to the temporal and spatial resolution of our microscope. The former is defined by $q_w = R/\mathcal{W}$, where \mathcal{W} is the Gaussian width of the lateral point spread function. The values of this cutoff in our experiments are typically larger than the mode number $q = 30$. On the other hand, the temporal cutoff is defined (as mentioned in the main text) by the value of \mathcal{Q} that satisfies $\frac{1}{2} \tau_{\mathcal{Q}} = 2\pi R/(v\mathcal{Q})$, where v is the effective velocity of the line scanning front, perpendicular to the scan direction. Therefore, q_{\max} needs to be less than \mathcal{Q} which typically has values greater than $q = 18$ in our experiments. Since q_c and \mathcal{Q} depend on the inferred values of κ and $\bar{\sigma}$, the constraints on the value of $q_{\max} \in (q_c, \min(q_w, \mathcal{Q}))$ are, in practice, checked *a posteriori* after a brute-force computation of $\mathbb{P}(q_{\max} | \mathbf{F}_{\Delta}, \mathbf{I})$ is obtained for a large range of values (from 5 to 40); see the Mathematica (Wolfram Research, Inc.) code in `DataAnalysis.nb` file of the Supplementary Material.

The same procedure of maximizing the posterior probability in Eq. (S.3.5) can be carried out for datasets \mathcal{D} that may include many other spectra measured on the same vesicle at different focal depths, or spectra obtained from distinct vesicles of the same lipid composition (that is, same value of κ), or both. Since every experimental datum $F_q(\Delta)$ is assumed to be completely independent of each other, this implies that the posterior probability over the entire data \mathcal{D} is given by a product of Eq. (S.3.5) over the different focal depths or different GUVs, or a mixture of the two, namely

$$\mathbb{P}(\mathbf{X} | \mathcal{D}, \mathbf{I}) \propto \prod_{\ell, \Delta} \exp\left[-\frac{\chi_{\Delta}^2(\kappa, \bar{\sigma}_{\ell})}{2}\right] \prod_{q=q_{\min}}^{q_{\max}} \frac{1}{\sqrt{2\pi}\Sigma_q(\Delta)}, \quad (\text{S.3.11})$$

where we omit, for brevity, the explicit dependence of both Σ_q and q_{\max} on ℓ that labels the different vesicles. The value of the upper bound q_{\max} is computed as before by the maximum of the posterior probability in Eq (S.3.9) for each individual spectra associated with (ℓ, Δ) .

References

- [1] Parolini, L. *et al.* Volume and porosity thermal regulation in lipid mesophases by coupling mobile ligands to soft membranes. *Nat. Commun.* **6**, 5948 (2015).
- [2] Angelova, M. I. Liposome Electroformation. In Luisi, P. L. & Walde, P. (eds.) *Giant Vesicles*, vol. 6 of *Perspectives in Supramolecular Chemistry*, chap. 3, 27–36 (John Wiley & Sons, Chichester, 1999).
- [3] Frenkel, D. & Smit, B. *Understanding Molecular Simulation: From Algorithms to Applications*. Computational science series (Elsevier Science, 2001).
- [4] Kikuchi, K., Yoshida, M., Maekawa, T. & Watanabe, H. Metropolis monte carlo method as a numerical technique to solve the fokkerplanck equation. *Chemical Physics Letters* **185**, 335 – 338 (1991).
- [5] Sanz, E. & Marenduzzo, D. Dynamic monte carlo versus brownian dynamics: A comparison for self-diffusion and crystallization in colloidal fluids. *The Journal of Chemical Physics* **132**, 194102 (2010).
- [6] Pécéréaux, J., Döbereiner, H. G., Prost, J., Joanny, J. F. & Bassereau, P. Refined contour analysis of giant unilamellar vesicles. *Eur. Phys. J. E* **13**, 277–290 (2004).
- [7] Yoon, Y.-Z. *et al.* Flickering analysis of erythrocyte mechanical properties: dependence on oxygenation level, cell shape, and hydration level. *Biophys. J.* **97**, 1606–15 (2009).
- [8] Faucon, J., Mitov, M. D., Méléard, P., Bivas, I. & Bothorel, P. Bending elasticity and thermal fluctuations of lipid membranes. *J. Phys. Fr.* **50**, 2389–2414 (1989).
- [9] Milner, S. T. & Safran, S. A. Dynamical fluctuations of droplet microemulsions and vesicles. *Phys. Rev. A* **36**, 4371–4379 (1987).
- [10] Abramowitz, M. & Stegun, I. *Handbook of Mathematical Functions* (Dover Publications Inc., New York, 1965).
- [11] Kardar, M. *Statistical Physics of Fields* (Cambridge University Press, Cambridge, 2007).
- [12] Henriksen, J. R. & Ipsen, J. H. Thermal undulations of quasi-spherical vesicles stabilized by gravity. *Eur. Phys. J. E* **9**, 365–74 (2002).
- [13] Sivia, D. S. & Skilling, J. *Data Analysis – a Bayesian tutorial* (Oxford University Press, Oxford, 2006), 2nd edn.